Study of photoelectrochemical conductivity mechanism and electrochemical impedance spectroscopy of bulk $CuInTe_2$ – electrolyte interface

Manorama G. Lakhe , Ashwini B. Rohom , Priyanka U. Londhe , Ganesh R. Bhand , Nandu B. Chaure

PII: S2468-0230(18)30119-6
DOI: 10.1016/j.surfin.2018.05.012
Reference: SURFIN 212

To appear in: *Surfaces and Interfaces*

Received date: 9 March 2018
Revised date: 22 April 2018
Accepted date: 28 May 2018

Please cite this article as: Manorama G. Lakhe , Ashwini B. Rohom , Priyanka U. Londhe , Ganesh R. Bhand , Nandu B. Chaure , Study of photoelectrochemical conductivity mechanism and electrochemical impedance spectroscopy of bulk $CuInTe_2$ – electrolyte interface, *Surfaces and Interfaces* (2018), doi: 10.1016/j.surfin.2018.05.012

H I G H L I G H T S

- $CuInTe_2$ (CIT) thin films were electrosynthesized on fluorine doped tin oxide at higher pH 4.
- CIT films were studied by photoelectrochemical (PEC) response and confirm the p-type conductivity of CIT films.
- Charge transport mechanism was studied by electrochemical impedance spectroscopy.
- Impedance measurement shows tunnel diode like behavior at higher frequencies whereas diffusion mechanism of ionic species dominated at lower frequencies.
- The science behind photoelectrochemical and impedance measurement is explained in details.

Study of photoelectrochemical conductivity mechanism and electrochemical impedance spectroscopy of bulk $CuInTe_2$ - electrolyte interface

Manorama G. Lakhe[a,b]*, Ashwini B. Rohom[b], Priyanka U. Londhe[b], Ganesh R. Bhand[b], Nandu B. Chaure[b]*

[a]Physical and Materials Chemistry Division, CSIR - National Chemical Laboratory, Pune, 411008 India

[b]Department of Physics, Savitribai Phule Pune University (Formerly University of Pune), Pune 411007, INDIA

*Corresponding author:

a. E-mail: lakhe.manorama@gmail.com

Tel: (+9120) 2590 2580; Fax: (+9120) 2590 2636

b. E-mail: n.chaure@physics.unipune.ac.in

Tel:(+9120) 2569 2678; Fax: (+9120) 2569 1684

ABSTRACT

$CuInTe_2$ (CIT) thin films were electrochemically deposited in an aqueous electrolyte on fluorine doped tin oxide (FTO) coated glass substrates for potentials ranging from - 0.6 V to - 0.9 V at pH 4. Films were annealed at 400 ^oC for 15 minutes in air ambient. Both as-deposited and annealed layers were characterized by various characterization techniques. The conductivity type of the CIT layers was studied by photoelectrochemical (PEC) response and solid–electrolyte interface by impedance spectroscopy. As-deposited samples confirmed amorphous nature of CIT in contrast to that of polycrystalline films obtained upon annealing. Three prominent reflections (1 1 2), (2 2 0)/(2 0 4) and (3 1 2)/(1 1 6) of chalcopyrite CIT were obtained upon annealing. The optical band gap values ~ 0.90 eV and 1.08 eV and ~ 0.88 eV and 1.01 eV were estimated for as-deposited and annealed CIT layers deposited at - 0.7 V and - 0.8 V respectively. The most prominent A_1 mode observed at 123 cm^{-1} in the Raman spectra of chalcopyrite CIT was shifted towards lower wavelengths due to the development of tensile strain. Very compact, well adhesive and void free globular layers were deposited at pH 4. The indium content was found to be increased with increasing the deposition potential which agrees well with the overpotential deposition of indium. Photoelectrochemical (PEC) study confirms the growth of p-type CIT layers. The negative resistance at higher frequency domain (3 MHz to 10 kHz) from electrochemical impedance spectroscopy (EIS) confirms the power/energy giving nature of CIT/electrolyte interface at higher frequency and diffusion mechanism of ionic species dominate at lower frequency region.

Keywords: Raman spectra, conductivity, impedance spectroscopy

1. Introduction

The study of solid – liquid interface has remained the topic of fascination to study the local crystallanity and charge storage mechanism in the field of energy storage and harvesting [1] which has shown significant impact on both the cost of device fabrication and energy storage. Various materials in the form of metal oxides, metal sulphides, composites and oxynitrides are used for energy storage [2-5] which offers easy and environmental friendly processes. $CuInTe_2$ (CIT) is one of the important direct band gap materials from chalcopyrite family reported for thermoelectric and solar cell applications [6-10]. In this paper this material is obtained by electrodeposition technique, but very few people have studied its solid-liquid interface [11]. So it becomes crucial to study the phenomenon related to solid – liquid interface to investigate electronic, photoelectrochemical, surface and morphological properties of the semiconductor material/electrode and to understand the physical processes, charge transport, mass transport, reaction kinetics, surface segregation and chemical stability [12]. The photoelectrochemical response (PEC) and electrical impedance spectroscopy (EIS) are effective and non-destructive tools to understand and visualize the various aspects of the aforementioned interfaces and ionic layers in the electrolyte and near the periphery of electrode and also to study the charge transport mechanism. Vijaykumar et al. [11] have worked on the electrodeposition process and reported three double layers: a space charge layer (1000 A^o), Helmholtz double layer (3 – 5 A^o) and Gouy – Chapman double layer (100 A^o). If a third phase such as an oxide film is present in the semiconductor electrode, charge can be stored in the interface between oxide and the substrate or even in the form of space charge layer. J. Gasiorowski et al. [13] have employed EIS measurement for poly[4,8-bis-substituted-benzo[1,2-b:4,5-b0]dithiophene-2,6-diyl-alt-4-substitutedthieno[3,4-b]thiophene-2,6-diyl] (PBDTTT-c) thin films to study the changes in

resistance and capacitance of the oxidized polymer. The semiconducting properties of electrochemically polymerized pyrrole-*N*-propionic acid (PPA) thin films in various supporting electrolyte was studied by Karazehir et al. [14] by EIS. The equivalent circuits for the obtained Nyquist and Bode plots were discussed thoroughly. Chemla et al. [15] have analyzed the different electrochemical processes occurring at semiconductor/electrolyte interface for p and n-type silicon in pure diluted HF solution under dark by using EIS. They have correlated a two-step charge transfer mechanism to the electrochemical processes involved in the reaction of Si substrate with HF. Bertoluzziet al. [16] have shown the importance and mechanism of charge transfer in terms of both direct hole transfer from valance band and indirect hole transfer via surface states for solar fuel production. Herraiz-Cardona et al. [17] have successfully employed EIS technique to determine the conductivity of p-type $CuGaO_2$ by fitting an equivalent circuit to the obtained EIS spectra and knowing the charge transport resistance, film thickness, geometrical area and porosity of the sample. In addition to all above parameters one more approach i.e. modulation of pore size of electrochemically etched p-type silicon in Polyethyleneglycol(PEG) additive by fast fourier transformation impedance spectroscopy (FFT-IS) is proposed by Quiroga-Gonzalez et al.[18]. Based on the physical phenomena at the solid-liquid interfaces several representations of the equivalent circuits have been used to explain the electrode – electrolyte interface.

The present work emphasizes on both material properties of CIT and CIT-electrolyte interface. CIT – electrolyte interface was studied by photoelectrochemical response (PEC) and electrochemical impedance spectroscopy (EIS) and discussed thoroughly in this paper. Imaginary impedance is measured versus real impedance over a wide range of frequency.

Comparative study of the as-deposited and annealed CIT films deposited at - 0.7 V and - 0.8 V is presented.

2. Experimental details

2.1 Materials used for synthesis of CIT thin films

Copper sulphate ($CuSO_4$) from Sigma - Aldrich, indium sulphate ($In_2(SO_4)_3$) from SRL and tellurium oxide (TeO_2) from Sigma – Aldrich of purity at least 99.9 % have been used for the experimentation. Citric acid is used as complexing agent. The above chemicals are dissolved in double distilled water. pH of the bath was adjusted with ammonia and NaOH.

2.2 Electrodeposition of CIT thin films

CIT thin films were electrodeposited for pH 4 at constant bath temperature 75 ^{o}C (± 1 ^{o}C) with continuous stirring at 150 rpm throughout the experiments. A conventional three-electrode system, consisting fluorine doped tin oxide (FTO) as working, graphite as counter and Ag/AgCl as reference electrode were used. Prior to the experiments, the substrates were thoroughly cleaned using double distilled boiled water, acetone and iso-propanol followed by few minutes ultra – sonication with iso-propanol. Potentiostat/galvanostat, Model Biologic SP 300 was used to perform the cyclic voltammetry analysis and electrodeposition of precursor layers and finally its photochemical and impedance analysis. The deposition potential was optimized by cyclic voltammetry (CV) experiments. The samples were electrodeposited in the range - 0.6 V to - 0.9 V and subsequently annealed in the muffle furnace in an air ambient at 400 ^{o}C for 15 minutes and used for characterization.

2.3 Characterization of CIT thin films

X- ray diffractometer, model Bruker D8 Advance, Germany of Cu Kα radiation with $\lambda = 0.154$ nm was used to study the structural properties. Raman spectrum was recorded with Invia

Renishaw Raman Microscope coupled with Philips CCD camera in the range 100 cm^{-1} to 300 cm^{-1}. Semiconductor laser of wavelength 785 nm was used as an excitation source. Optical study was carried out by JASCO UV-VIS-NIR Spectrophotometer model V-670. JEOL JSM – 6360 A SEM/EDAX at accelerating voltage 20 kV and probe current 1 nA was used to study the surface morphology and elemental composition. The conductivity type was studied by photoelectrochemical (PEC) measurements. The solid-liquid interface was studied by electrochemical impedance spectroscopy (EIS). Three electrode system was used for both PEC as well as EIS analysis. The PEC and EIS study was carried out at room temperature in 1M KCl and1M NaOH electrolytes respectively. PEC response of both as-deposited and annealed CIT samples was recorded with constant applied bias of -100 mV under illumination of white light source of intensity 100 mW/cm^2.

3. Results and discussion

3.1 Cyclic voltammetry

The cyclic voltammogram recorded on FTO substrate at 75 ^oC for stirred solution at ~ 150 rpm for co-deposition of Cu, In, Te with citric acid at pH 4 is shown in figure 1.

Cathodic and anodic scans are marked by forward (black) arrows, and reverse (red) arrows, respectively. The cathodic current increased from - 0.4 V due to the metallic deposition of copper and or tellurium on the substrate. Plateau region observed between - 0.65 V to - 0.85 V is the suitable growth potential for $CuInTe_2$. Sharp rise in current after - 0.95 V is associated with the hydrogen evolution along with nonstoichiometric deposition of CIT. The anodic scan shows the similar trend in the current upto - 0.80 V. Below - 0.80 V the anodic current becomes positive corresponds to oxidation process. The anodic peaks exhibited at - 0.65 V and - 0.47 V are corresponds to the stripping of indium and copper, respectively. The cross over observed

around - 0.40 V could be due to the metallic deposition of copper/tellurium. The anodic peak observed around + 0.40 V is associated with stripping of Te. The number of CV measurements was performed to observe the repeatability of the curve to optimize the closest deposition potential of CIT. The co-deposition of Cu, In and Te is made possible by using citric acid as complexing agent which drives the deposition potential of different elements closer by changing the activity of the respective element by forming the complex with them.

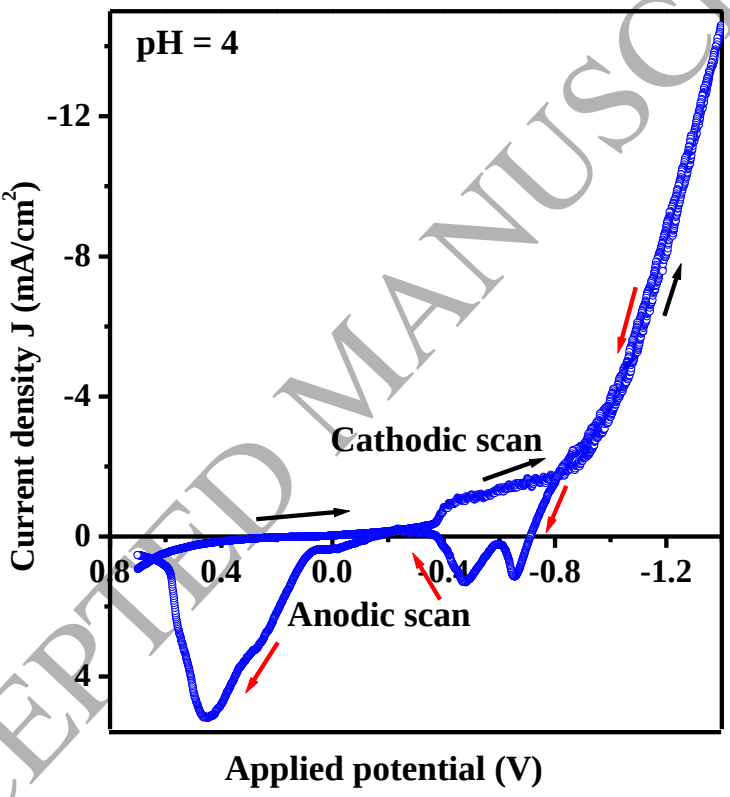

Figure 1 The cyclic voltammogram recorded on FTO substrate at 75 ^{o}C for stirred solution at ~ 150 rpm for co-deposition of Cu, In, Te with citric acid at pH 4.

From cyclic voltammetry results the co-deposition of CIT falls in the range - 0.6 V to - 0.9 V. Reaction mechanism of CIT in details is reported elsewhere [10].

3.2 X-ray diffraction

Figure 2 shows the X-ray diffraction pattern of as-deposited and annealed CIT thin films. The dark circles (●) in figure 2 are related to the substrate (FTO) peaks. As-deposited films (a) and (c) deposited at - 0.7 V and - 0.8 V respectively shows amorphous nature.

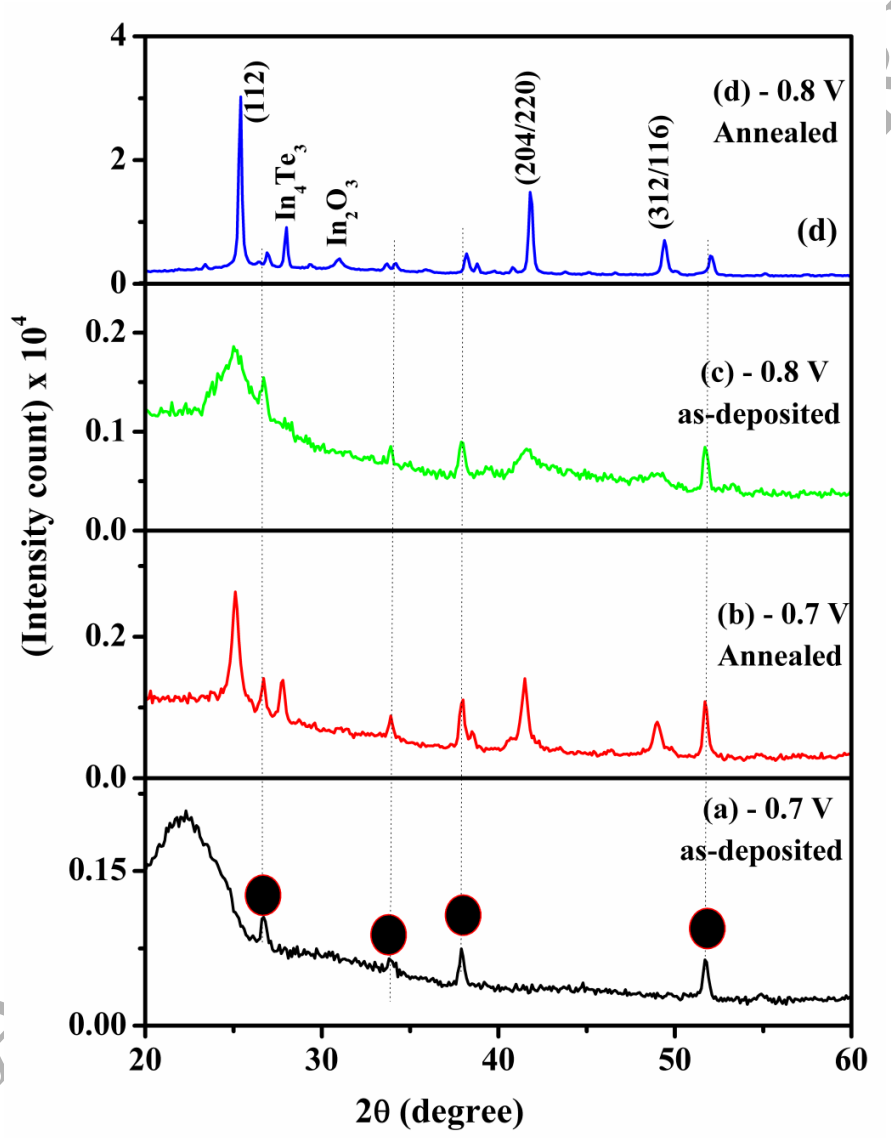

Figure 2 X-ray diffraction patterns of as-deposited and annealed CIT thin films.

Upon annealing the same films [fig. 2(b) and (d)] sharp reflections at an angle 2θ = 25.09°, 41.47° and 49.03° corresponds to (1 1 2), (2 0 4) / (2 2 0) and (3 1 2) / (1 1 6) of tetragonal structure of CIT [JCPDS file no. 34-1498] are observed. Highly polycrystalline CIT was obtained upon annealing the sample deposited at -0.8 V. Secondary phases of In_4Te_3 at 2θ = 27.46°, corresponds to (3 1 1) plane [JCPDS file no. 83-0043] and In_2O_3 at 2θ = 27.46° (222) [JCPDS file no. 22-0336] are also observed in both the annealed samples.

The secondary phases of In_4Te_3 and In_2O_3 attributed upon annealing can be removed by optimizing the annealing temperature and duration. The crystallite size is calculated by using the Debey Scherrer classical equation [10] and was found to be ~ 4 - 5 nm for the as-deposited samples and for 36 nm and 118 nm for annealed samples deposited at - 0.7 V and - 0.8 V, respectively.

3.3 Raman spectroscopy

Figure 3 shows the Raman spectra of as-deposited and annealed CIT films deposited at - 0.7 V and - 0.8 V.

The noticeable change in Raman spectra is observed for the as-deposited samples with respect to deposition potential. It is clearly observed that overall background intensity is more and peaks are quite distinguishable for the as-deposited sample deposited at - 0.7 V as compared to the sample deposited at - 0.8 V. This could be due to the presence of some Raman active surface states/impurities in that sample which enhances the surface Raman resonance. The details of the modes are summarized in Table 1. Upon annealing, the FWHM of A_1 mode was decreased in both the samples and Raman modes became very sharp. The distinct Raman modes A_1 at 120 cm^{-1} [19], B^3_1 at 141 cm^{-1} [20], E_5 and/ or $B_2{}^3$ (TO) at 156 -171 cm^{-1} [20], longitudinal optical

(LO) B_2 and/or E (LO) mode at 182 cm^{-1} [20], E (LO) at 220 cm^{-1} [21] and E & B_2 at 267 cm^{-1} [19] were observed in annealed samples and remaining modes were silent.

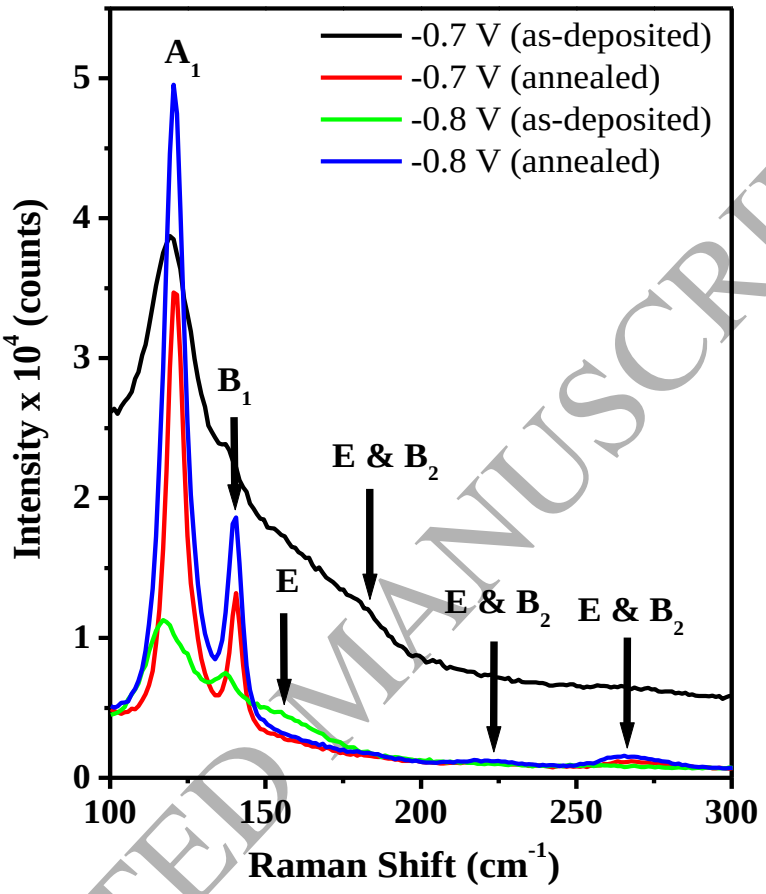

Figure 3 Raman spectra of as-deposited and annealed CIT thin films deposited at - 0.7 V and - 0.8 V.

The peak position of A_1 mode generally observed at 123 cm^{-1} was found to be shifted at 120 cm^{-1}, 117 cm^{-1} in as-deposited samples deposited at -0.7 V and -0.8 V respectively. In annealed samples, it was shifted to 121 cm^{-1}. This red shift in the Raman modes is because of the development of tensile strain [22, 23] and decrease in red shift after annealing indicates the reduction in strain.

3.4 Optical properties

The plot of $(\alpha h\nu)^2$ verses energy ($h\nu$) for as-deposited and annealed CIT samples at 400 ^oC for 15 minutes is shown in figure 4. The band gap of the CIT films is found to be a function of deposition potential and varies from 0.98 eV to 1.08 eV [9,10] for as deposited films deposited at - 0.7 V and - 0.8 V and decreases upon annealing from 0.88 eV to 1.01 eV. The change in band gap is associated with the enhancement in particle size [24] as well as presence of secondary phases.

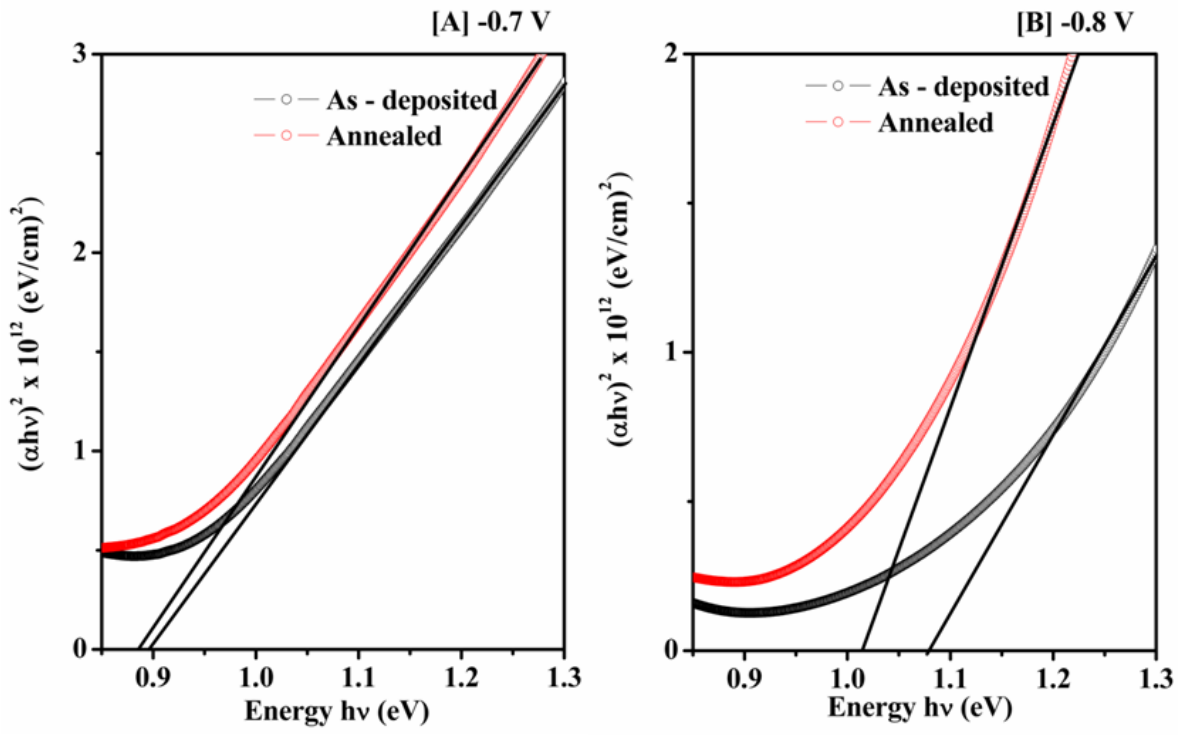

Figure 4 Plot of $(\alpha h\nu)^2$ verses Energy ($h\nu$) for as-deposited and annealed CIT films at 400 ^oC for 5 minutes deposited at (A) -0.7 V and (B) -0.8 V.

3.5 Scanning electron microscopy (SEM)

The surface morphology of as-prepared CIT films deposited from -0.6 V to -0.9 V and annealed CIT films deposited for - 0.7 V and - 0.8 V is shown in figure 5.

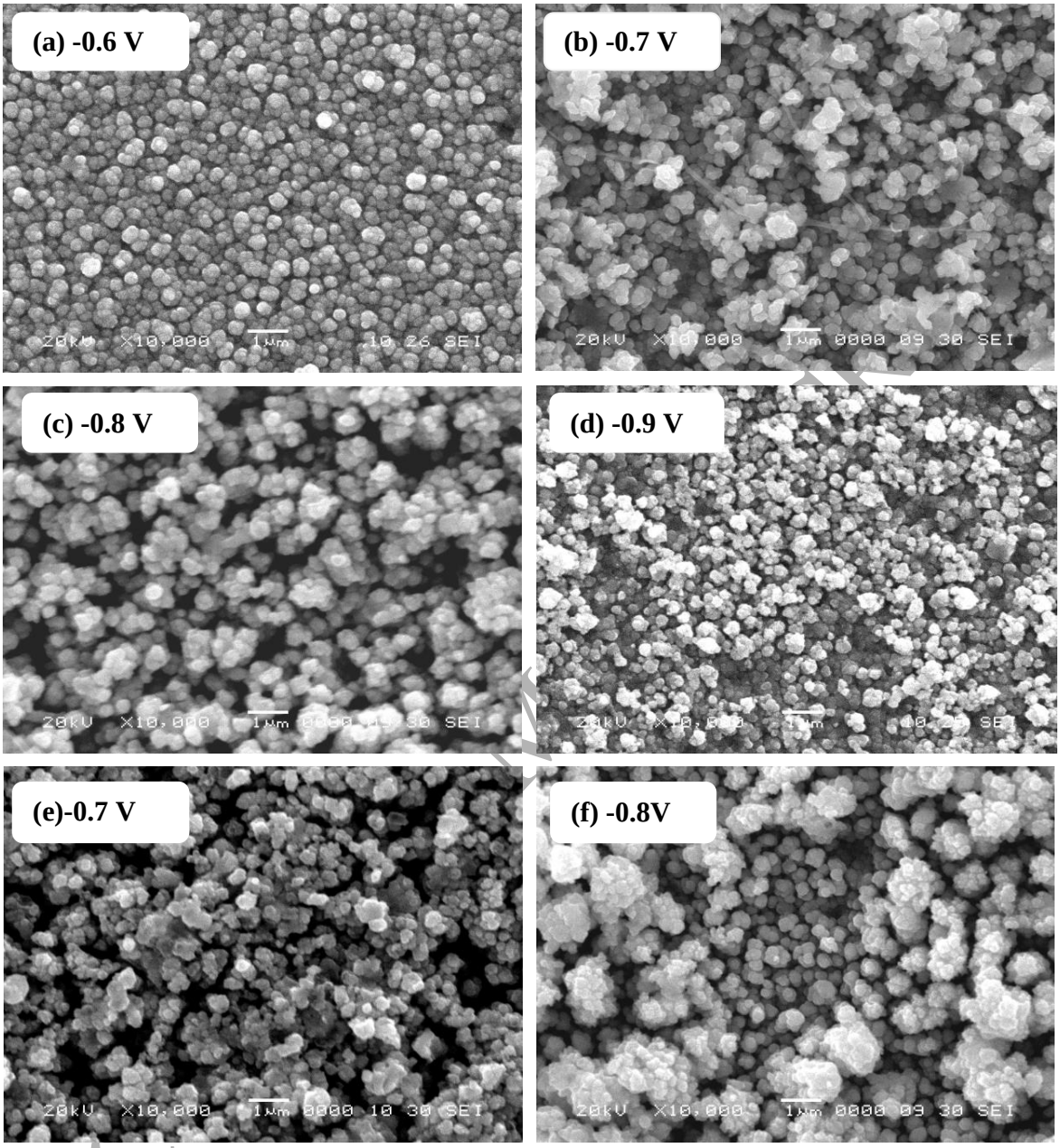

Figure 5 SEM Images of as-deposited CIT films deposited at (a) - 0.6 V, (b) - 0.7 V, (c) - 0.8 V and (d) - 0.9 V; and annealed CIT films at 400 ^{o}C for 15 minutes deposited at (e) - 0.7 V and (f) - 0.8 V respectively.

It is observed that all samples were compact and well adherent to the substrate. A clear change in surface morphology for as-prepared samples can be seen in fig.5 ((a) to (d)). Spherical grains

with nearly uniform size were observed for the metallic film deposited at lower potential - 0.6 V (fig. 5 (a)). Comparatively large grains with agglomeration were noticed for the deposition potential - 0.7 V (fig. 5 (b)) and - 0.8 V (fig. 5 (c)). The particle size was found to be decreased for the sample deposited at - 0.9 V (fig. 5 (d)) and could be due to the deposition of metallic indium rich film. We further observed that the films deposited at - 0.6 V and - 0.9 V were evaporated during the annealing process. The grain size has been found to be increased for the annealed samples deposited at - 0.7 V (fig. 5 (e)) and - 0.8 V (fig. 5 (f)). Small particles are agglomerated to form the cluster of size 2 μm; which could be helpful for the charge transport in the device.

3.6 Energy dispersive X-ray analysis (EDAX)

Figure 6 shows the EDAX pattern of as-deposited and annealed CIT films deposited at - 0.8 V and elemental compositional analysis of all as-prepared and annealed CIT films is summarized in table 2.

Tellurium rich film was-deposited at growth potential -0.6 V and the content of Te decreased systematically for the films deposited at higher potential. The content of indium was also found to be increased for the films deposited at higher potentials. The Cu/In ratio for as-prepared films was systematically decreased with increase in deposition potential which is proposed for high efficiency solar cell [9, 19]. Upon annealing the CIT layers deposited at - 0.7 V and - 0.8 V, the atomic percentage concentration of Cu, In and Te was determined ~ 17, 25 and 58 and 16, 36 and 48 respectively. Indium rich film is deposited at - 0.8 V with appropriate control on Cu/In ratio. The Te/(Cu+In) ratio decreased systematically with increase in deposition potential and upon annealing also which agrees well with XRD results.

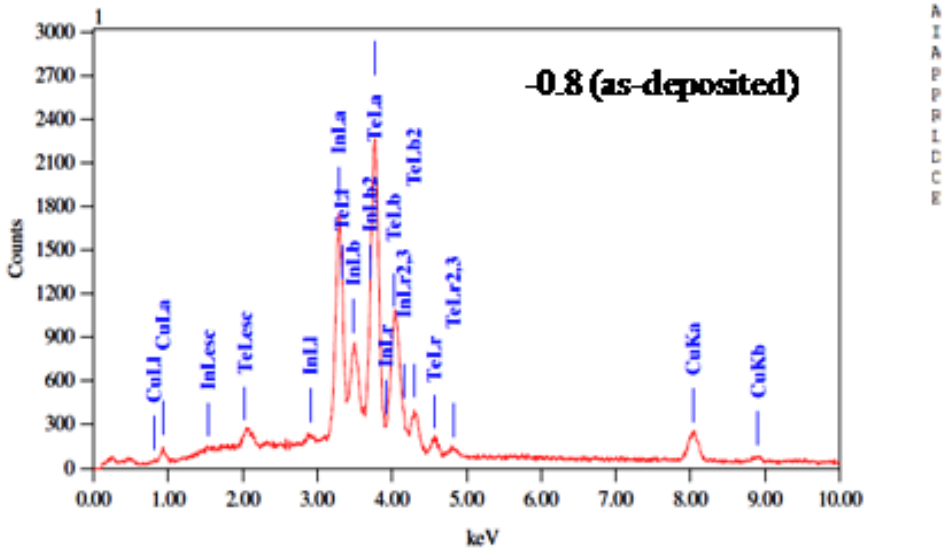

ZAF Method Standardless Quantitative Analysis
Fitting Coefficient : 0.3773

Element	(keV)	mass%	Error%	At%	Compound	mass%	Cation	K
Cu K	8.040	9.91	0.83	17.54				10.9102
In L	3.285	31.43	0.38	30.77				36.6307
Te L	3.768	58.66	0.56	51.69				52.4590
Total		100.00		100.00				

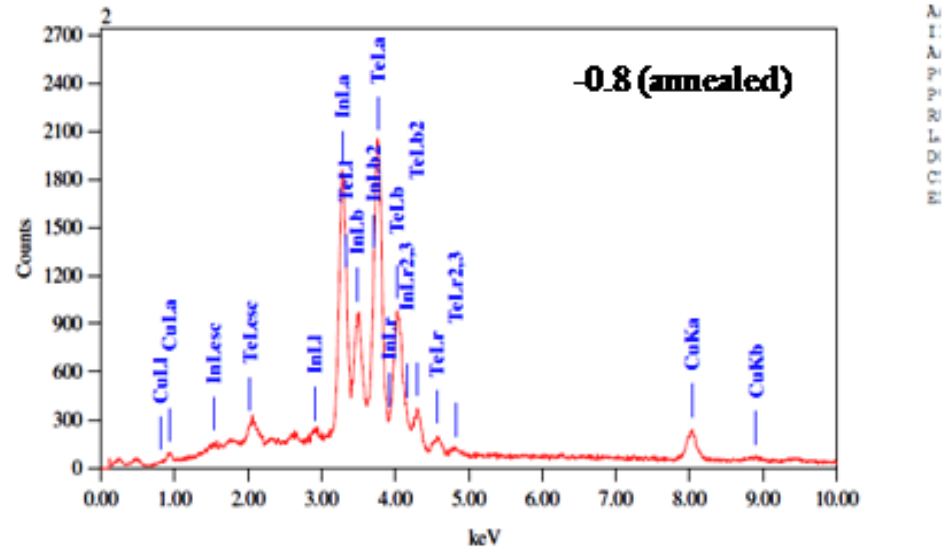

ZAF Method Standardless Quantitative Analysis
Fitting Coefficient : 0.4616

Element	(keV)	mass%	Error%	At%	Compound	mass%	Cation	K
Cu K	8.040	9.19	1.11	16.29				10.0692
In L	3.285	36.16	0.51	35.47				41.9483
Te L	3.768	54.65	0.76	48.24				47.9825
Total		100.00		100.00				

Figure 6 Energy dispersive X-ray spectra of as-deposited and annealed CIT samples deposited at -0.8 V.

3.7 Photoelectrochemical (PEC) study

Photoelectrochemical (PEC) study is one of the important tools to study the photocatalytic and photoelectrochemical water splitting applications [25 - 36] as well as to study photo effects for energy conversion [37] and the electrical conductivity type [38, 39]. One of the authors Momini et al. have rigorously studied this aspect for number of systems [25 - 27, 29, 30, 32, 34] with various dopants to improve the phocatalytic activity for water splitting applications under dark and illuminated condition with light chopping. When semiconductor surface under examination is immersed in electrolytic solution, electron transfer takes place in order to equilibrate the Fermi energy of the semiconductor and redox/chemical potential of the electrolyte. The charge imbalance in the semiconductor interface as that of the bulk produces the space charge layer at the interface whereas at electrolyte side the formation of densely packed Helmholtz double layer followed by Gouy-Chapman layer. Under applied bias the Fermi energy of the semiconductor and chemical potential of electrolyte shifts and current flows through the circuit. Under illumination the gap between Fermi energy and chemical potential further increases/decreases and current either increases towards negative side or positive side. In case of p-type semiconductor current increases towards negative side since under illumination the increase in current is due to the minority carriers [37-39] and electrons are the minority carriers in p-type semiconductors. When semiconductor – electrolyte interface is irradiated with light, mainly it is absorbed in the material and two phenomena takes place and importantly absorption of light over a spatial extent mainly depends on the absorption coefficient of the material. The electrons can be transferred into conduction band through the photoexcitation of semiconductor electrode itself and photoexcitation of redox couple.

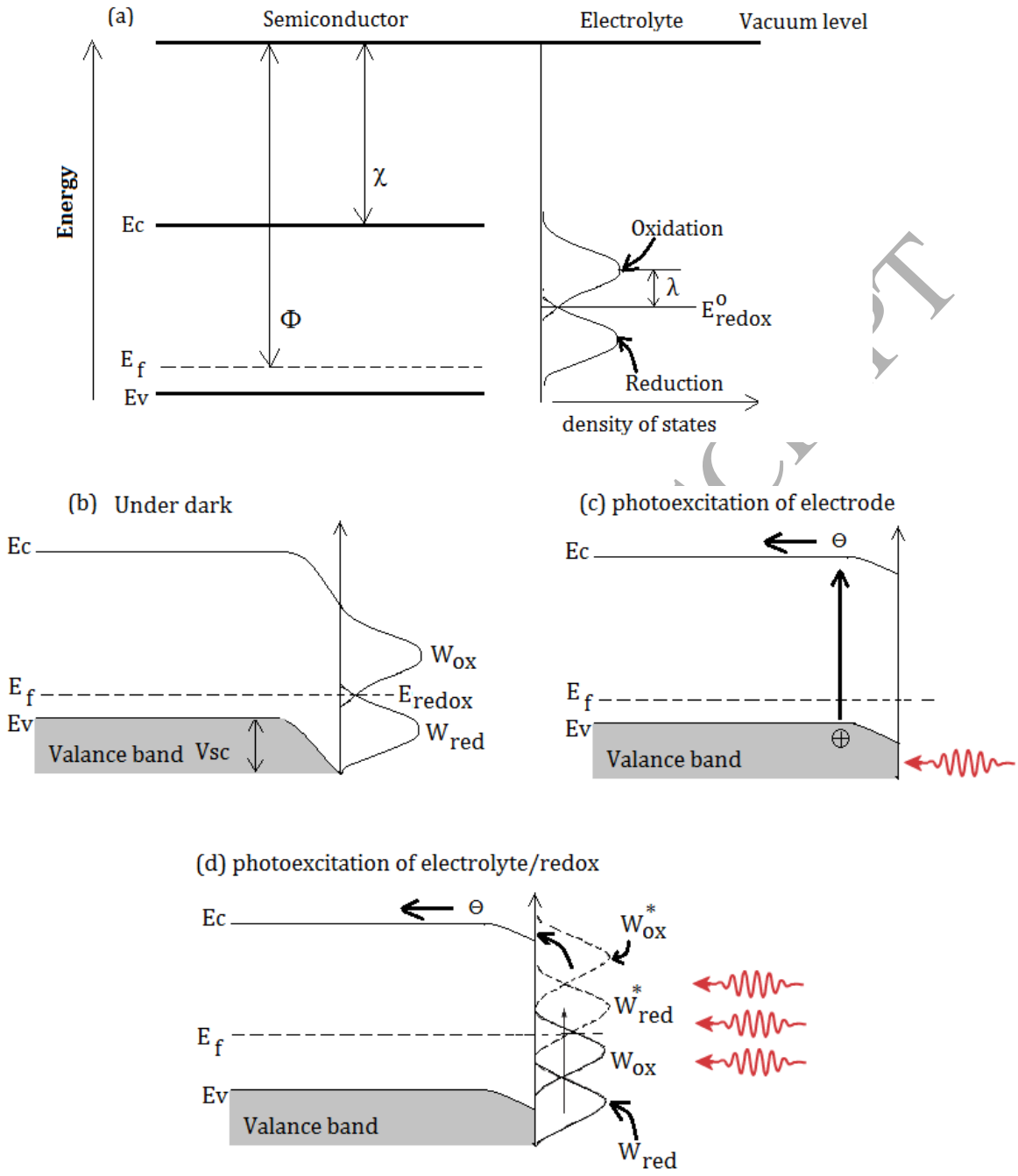

Figure 7 Schematic representation of solid-electrolyte interface. Figure (a) represents the top of the valance band edge energy level (Ev), bottom of the conduction band edge energy level (Ec), Fermi energy (E_f) of p-type semiconductor and redox potential/energy of electrolyte with respect to vacuum level separately. (b) Shows the band bending of the p-type semiconductor kept in contact with electrolyte to equilibrate the Fermi energy of a semiconductor and redox potential of electrolyte. (c) The photoexcitation of p-type semiconductor electrode. (d) Represents the photoexcitation of electrolyte.

In case of semiconductor electrode, electron-hole pairs will be generated only when it is illuminated with light source having energy equal to or greater than the bandgap of the semiconductor material and we have used white light source so entire visible spectra is covered. Whereas in case of semiconductor-electrolyte, the carriers will be created in the depletion region via oxidation and separated by the field (drift currents), in present case electrons are driven to the surface while positive ion carriers are forced towards electrolyte. Additionally, diffusion of carriers in the quasi-neutral region can also takes place even in dark which is also observed in present EIS results where diffusion mechanism is dominant at low frequencies. Although the diffusion length of these electron-hole pairs can be calculated experimentally; this is not the scope of present work. Guady et al. [36] have also explained the water splitting mechanism in terms of energy band diagram in case of n-type GaN-electrolyte interface. Lewis et al. [37] have thoroughly studied the photo-effects at the semiconductor-liquid interfaces and explained the mechanism of separation of minority carries at semiconductor-electrolyte interface under illumination. In present case, the schematic representation of solid-electrolyte interface for photochemical response is shown in figure 7. Figure 7 (a) represents the top of the valance band edge energy level (*Ev*), bottom of the conduction band edge energy level (*Ec*), Fermi energy (E_F) of p-type semiconductor and redox potential/energy of electrolyte with respect to vacuum level separately. Figure 7 (b) shows the band bending of the p-type semiconductor kept in contact with electrolyte to equilibrate the Fermi energy of a semiconductor and redox potential of electrolyte. The terms W_{ox} and W_{red} shows the oxidation and reduction distribution function. Figure 7 (c) shows the photoexcitation of p-type semiconductor electrode and figure 7 (d) represents the photoexcitation of electrolyte. The terms W^*_{ox} and W^*_{red} shows the shift in oxidation and reduction distribution function under illumination from that of the dark. While explaining the

photoelectrochemical and photocatalytic properties of organic p and n-type semiconductor, Zhang et al. [35] has given the schematic representation of n and p-type monolayer – electrolyte interface under dark whereas n/p and p/n - type bilayer-electrolyte under illumination. In present case; interface is CIT- electrolyte and CIT is not either in the form of monolayer or it is not a combination of p/n bilayer instead it is a bulk material; so our schematic deviates from that of the reported data. What we have shown in case of p-type CIT - electrolyte interface is exactly shown oppositely for n-type GaN-elctrolyte interface since band bending of n-type semiconductor with that of electrolyte will be upward direction to adjust the Fermi level of n-type semiconductor and redox/chemical potential of electrolyte. The charges will be transferred into ionic species in electrolyte via valance band of the semiconductor under illumination and the position of oxidation and reduction potential will shift towards downward direction and hence the reduction potential.

In present study, as-deposited and annealed samples of CIT deposited at - 0.7 V and - 0.8 V were subjected for PEC study and it was carried out at room temperature in 1M KCl electrolyte. The photo response curve recorded with constant applied bias of -100 mV under illumination of white light source of intensity 100 mW/cm^2, in terms of photocurrent density (J) verses time 't' is measured and shown in figure 8. The spectrum obtained for as-deposited samples is not shown due to noisy signal. It is observed that the photocurrent of both the samples increased towards the negative side under illumination due to two processes. As shown in figure 7 (c) and figure 7 (d) i) electrons are excited from valance band to the conduction band of bulk CIT and ii) oxidation of ionic species from double layers formed near the solid electrolyte, donates the electrons in the conduction band of the CIT and current increases in the negative direction. The present data is compared with the reference data with photochemical response of p-type CIS thin films [39].

The photocurrent increased towards negative direction confirms the p – type conductivity of CIT films.

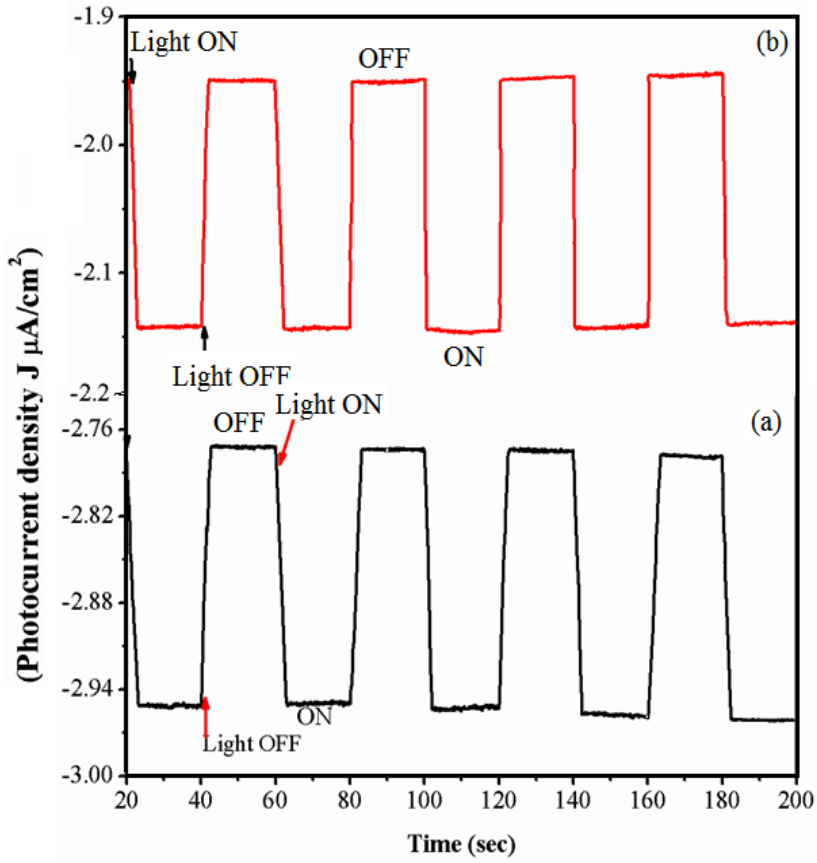

Figure 8 Photoelectrochemical (PEC) response of annealed CIT films at 400 ^{o}C for 15 minutes deposited at (a) -0.7 V and (b) – 0.8 V.

3.8 Electrochemical impedance spectroscopy (EIS)

Electrochemical impedance spectroscopy of CIT samples was carried out to understand the solid (semiconductor) – liquid interface in 1 M NaOH solution having pH 14 for a frequency range 3 MHz to 1 Hz. The measured imaginary impedance (Z') is plotted against real impedance (Z) and shown in figure 9 (A). The equivalent circuit for the plot is depicted in figure 9 (B). R_s is the series resistance arises from solution, film, wire and contact resistances, C_{dl} is the double layer

capacitance at semiconductor-electrolyte interface, R_{ct} is the charge transfer resistance from the ionic species and W is the Warburg coefficient which is created due to the diffusion of ionic species also called Warburg diffusion impedance. Value of '*W*' is high at lower frequencies and hence diffusion of ionic species is dominant at low frequencies. Our equivalent circuit well agreed with the literature data which is explained by Cesiulis et al. [40] except negative resistance at higher frequency.

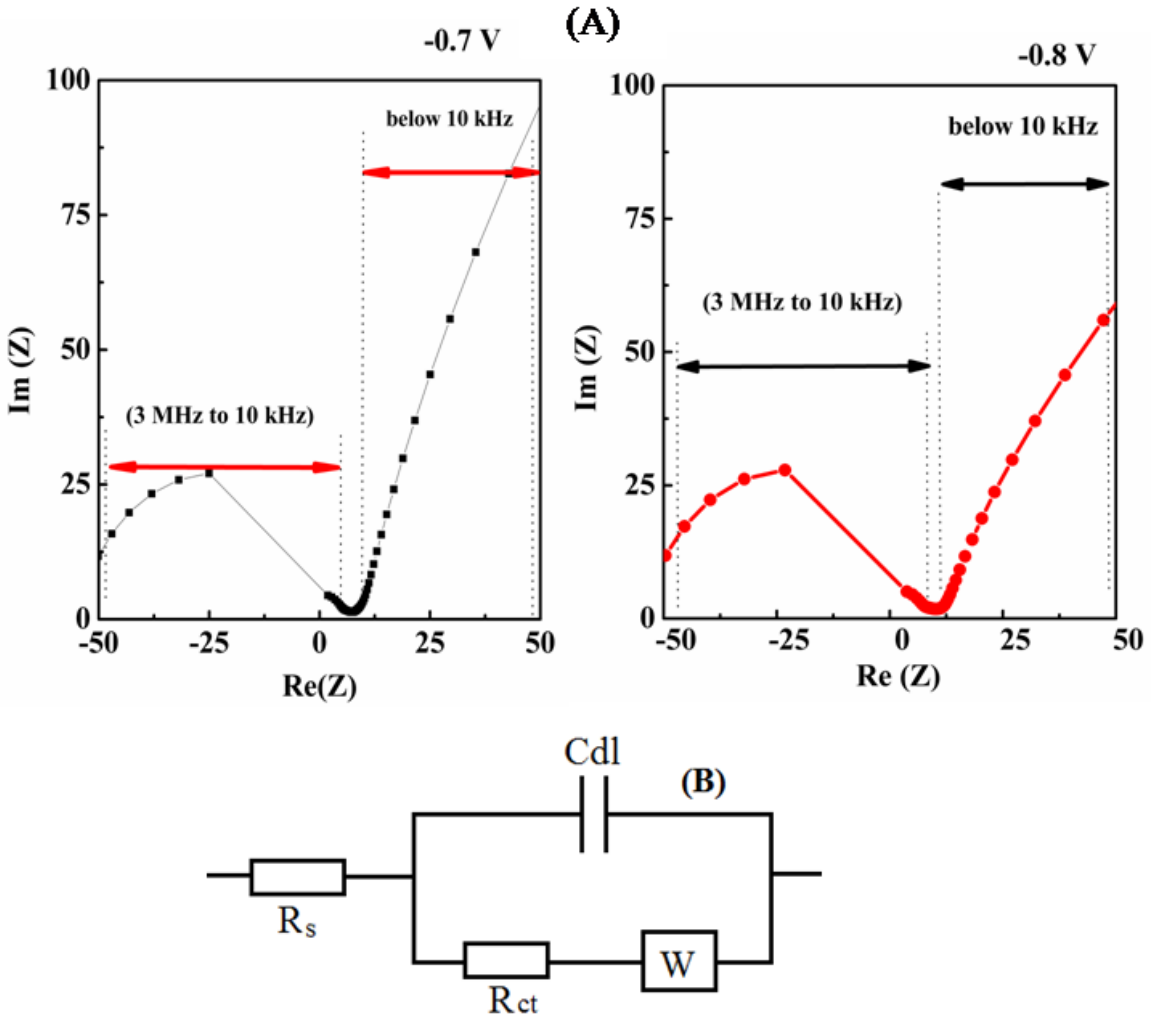

Figure 9 Impedance spectroscopy of annealed CIT films at 400 ^{o}C for 15 minutes deposited at (a) -0.7 V and (b) -0.8 V respectively.

Also one can change the equivalent circuit by replacing the double layer capacitance (C_{dl}) and Warburg coefficient (*W*) with constant phase element (*CPE*) which arises due to uneven distribution in microscopic material properties. The impedance due to chemical phase element is given by the equation [14, 40],

$$Z_{CPE} = \frac{1}{Q(jw)^n} \quad (1)$$

where *'Q'* constant '*n'* is related to the phase angle and varies in such a way that $0 < n < 1$ and shows resistive, capacitive and diffusion processes. When *'W'* is not placed in the circuit, the exponent values of constant phase element (*CPE*) approaches 0.5 and is indication of a diffusion controlled process. For a perfect capacitor the value of exponent is nearly 1 and the phase angle approaches 90°, which is the phase angle for a capacitor.

The present EIS data, CIT-electrolyte interface system [fig. 9 (A)] is compared with tunnel diode since it shows negative real resistance for higher frequencies just like tunnel diode shows negative resistance over particular region of current-voltage curve and makes it useful in oscillator circuit. The negative resistance at higher frequency region is mainly due to transfer of electrons via space charge region because of their fast response due to high mobility and negligible mass. Basically Soestbergen et al. [41] proposed the three different time scale to analyze the transient response of electrochemical cell with respect to current mainly, (i) the capacitive charging of the electroneutral bulk region is followed by Debye time, (ii) formation of the diffuse layer by harmonic time scale and (iii) the redistribution of ions across the cell takes place over diffusion time scale. The present EIS data for low frequency region shows the harmonic time scale and diffusion time scale since warburg element (W) is present due to formation of diffusion layers and redistribution of ionic species dominated at low frequency.

In general faradic current [42] for applied potential '*E*' is given by the following equation

$$i_f = nFAk_f\, C(0) \qquad (2)$$

where 'n' is the number of electrons, 'F' is the faraday constant, 'A' is the electrode surface area, 'k_f' is the rate constant and *C(0)* is the surface concentration of the electroactive species.

Depending upon the values of R_s, C_{dl}, R_{ct} and W nature of plot of Z' verses Z deviates from the ideal circuit. Thus by using EIS tool, charge transport mechanism at electrode/electrolyte interface over a wide frequency region can be studied.

4. Conclusions

Compact and well adherent CIT thin films were deposited successfully by electrodeposition technique at pH 4. Tellurium rich films were deposited at -0.6 V and its concentration systematically decreased with increase in deposition potential whereas indium concentration increased with increase in deposition potential. Highly crystalline CIT films were obtained upon annealing for growth potential -0.8 V. The secondary peaks of In_4Te_3 were revealed in the above samples along with materials peak. The red shift observed in the Raman spectra was due to the development of tensile strain which was decreased upon annealing. The optical bandgap obtained for as-deposited CIT thin films was in the range of 0.90 eV and 1.08 eV and upon annealing it was found to be ~ 0.88 eV and 1.01 eV for the films deposited at -0.7 V and -0.8 V respectively. The grain size of CIT layers deposited at -0.8 V and annealed at 400 ^{o}C was found to be 2μm. Photocurrent conduction mechanism of solid/liquid interface is thoroughly discussed in this paper and photoelectrochemical (PEC) study confirms the p-type conductivity of CIT films. Impedance measurement shows tunnel diode like behavior at higher frequencies whereas diffusion mechanism of ionic species is dominant at lower frequencies. This work helps to understand in situ deposition mechanism during the deposition of bulk material, its microstructure and conductivity type which are the governing factors for various applications.

Acknowledgement

One of the authors ML is thankful to University Grant Commission (UGC) for UGC-BSR fellowship. DST SERB is deeply acknowledged for SERB NPDF.

References

[1] P. Simon, Y. Gogotsi, Materials for electrochemical capacitors, nature materials 7 (2008) 845.

[2] M. K. Tian, W. F. Shangguan, J. Yuan, S. J. Wang, Z. Y. Ouyang, Promotion effect of nanosized Pt, RuO_2 and NiO_x loading on visible light-driven photocatalysts $K_4Ce_2M_{10}O_{30}$ (M = Ta, Nb) for hydrogen evolution from water decomposition, Sci Tech Adv Mater 8 (2007) 82 – 88.

[3] N. Z. Bao, L. M. Shen, T. Takata, K. Domen, Self-Templated Synthesis of Nanoporous CdS Nanostructures for Highly Efficient Photocatalytic Hydrogen Production under Visible Light, Chem. Mater. 20 (2008) 110 – 117.

[4] K. Maeda, K. Teramura, N. Saito, Y. Inoue, K. Domen, Improvement of photocatalytic activity of $(Ga_{1-x}Zn_x)(N_{1-x}O_x)$ solid solution for overall water splitting by co-loading Cr and another transition metal, J. Catal. 243 (2006) 303 – 108.

[5] J. Choi, S.Y. Ryu, W. Balcerski, T. K. Lee, M. R. Hoffmann, Photocatalytic production of hydrogen on Ni/NiO/$KNbO_3$/CdS nanocomposites using visible light, J. Mater. Chem. 18 (2008) 2371–78.

[6] R. Liu, L. Xi, H. Liu, X. Shi, W. Zhang, L. Chen, Ternary compound $CuInTe_2$: a promising thermoelectric material with diamond-like structure, Chem. Commun., 48 (2012) 3818–3820.

[7] V. Kucek, C. Drasar, J. Kasparova, T. Plechacek, J. Navratil, M. Vlcek, L. Benes, High-temperature thermoelectric properties of Hg-doped $CuInTe_2$, Journal of Applied Physics, 118 (2015) 125105

[8] Y. Luo, J. Yang, Q. Jiang, W. Li, D. Zhang, Z. Zhou, Y. Cheng, Y. Ren, X. He, Progressive Regulation of Electrical and Thermal Transport Properties to High-Performance $CuInTe_2$ Thermoelectric Materials, Advanced Energy Materials, 6 (2016) 1600007

[9] T. Mise, T. Nakada, Narrow-bandgap $CuIn_3Te_5$ thin-film solar cells, Prog Photovolt Res Appl 12 (2013) 754-759.

[10] M. Lakhe, N. B. Chaure, Characterization of electrochemically deposited $CuInTe_2$ thin films for solar cell applications, Solar Energy Materials & Solar Cells123 (2014) 122-129.

[11] A. Vijayakumara, T. Dub, K. B. Sundaram, Characterization of copper indium ditelluride/electrolyte interface utilizing electrochemical impedance spectroscopy, Applied Surface Science 242 (2005) 168- 176.

[12] J. Nowotny, C. C. Sorrell, T. Bak, L. R. Sheppard, Solar – hydrogen: Unresolved problems in solid - state science, Solar Energy 78 (2005) 593–602.

[13] J. Gasiorowski, A. I. Mardare, N. S. Sariciftci, A. W. Hassel, Characterization of local electrochemical doping of high performance conjugated polymer for photovoltaics using scanning droplet cell microscopy Electrochimica Acta 113 (2013) 834– 839.

[14] T. Karazehir, M. Ates, A. Sezai Sarac, Mott–Schottky and Morphologic Analysis of Poly(Pyrrole-N-Propionic Acid) in various electrolyte systems Int. J. Electrochem. Sci. 10 (2015) 6146 – 6163.

[15] M. Chemla, J. F. Dufreche, I. Darolles, F. Rouelle, D. Devilliers, S. Petitdidier, D. Levy, Bias voltage dependent electrochemical impedance spectroscopy of p- and n-type silicon substrates, Electrochimica Acta 51 (2005) 665–676.

[16] L. Bertoluzzi, P. Lopez-Varo, J. A. Jimenez Tejada, J. Bisquert, Charge transfer processes at the semiconductor/ electrolyte interface for solar fuel production: insight from impedance spectroscopy, J. Mater. Chem. A 4 (2016) 2873.

[17] I. Herraiz-Cardona, F. Fabregat-Santiago, A. Renaud, B. Julian-Lopez, F. Odobel, L. Cario, S. Jobic, S. Gimenez, Hole conductivity and acceptor density of p-type $CuGaO_2$ nanoparticles determined by impedance spectroscopy: The effect of Mg doping, Electrochimica Acta 113 (2013) 570– 574.

[18] E. Quiroga-Gonzalez, J. Carstensen, C. Glynn, C. O. Dwyer, H. Foll, Pore size modulation in electrochemically etched macroporous p-type silicon monitored by FFT impedance spectroscopy and Raman scattering, Phys. Chem. Chem. Phys. 16 (2014) 255.

[19] T. Mise, T. Nakada, Low temperature growth and properties of Cu-In-Te based thin films for narrow bandgap solar cellsThin Solid Films 518 (2010) 5604-5609.

[20] M. R. Ananthan, S. Kasiviswanathan, Growth and characterization of stepwise flash evaporated $CuInTe_2$ thin films, Solar Energy Materials & Solar Cells 93 (2009) 188 – 192.

[21] C. Rincon, S. M. Wasim, G. Marin, E. Herandez, J. M. Delgado, J. Galibert, Raman spectra of $CuInTe_2$, $CuIn_3Te_5$ and $CuIn_5Te_8$ ternary compoundsJournal of Applied Physics 88 (2000) 3439 – 3444.

[22] I. D. Wolf, Micro-Raman spectroscopy to study local mechanical stress in silicon integrated circuits, Semicond Sci Technol 11 (1996) 139-154.

[23] S. Sahoo, G. L. Sharma, R. S. Katiyar, Raman spectroscopy to probe residual stress in ZnO nanowire, J Raman Spectrosc 43 (2012) 72-75.

[24] N. B. Chaure, S. Bordas, A. P. Samantilleke, S. N. Chaure, J. Haigh, I. M. Dharmadasa, Investigation of electronic quality of chemical bath deposited cadmium sulphide layers used in thin film photovoltaic solar cells, Thin Solid Films 437 (2003)10-17.

[25] M. M. Momeni, Y. Ghayeb, M. Shafiei, Preparation and characterization of CrFeWTiO_2 photoanodes and their photoelectrochemical activities for water splitting, Dalton Trans., 46 (2017) 12527.

[26] M. M. Momeni, M. Mirhosseini, M. Chavoshi, Growth and characterization of Ta_2O_5 nanorod and WTa_2O_5 nanowire films on the tantalum substrates by a facile one-step hydrothermal method, Ceramics International, 42 (2016) 9133-9138.

[27] M. Momeni, M. Mirhosseini, M. Chavoshi, A. Hakimizade, The effect of anodizing voltage on morphology and photocatalytic activity of tantalum oxide nanostructure, Journal of Materials Science: Materials in Electronics , 27 (2016) 3941-3947.

[28] T. Hisatomi, J. Kubota, K. Domen, Recent advances in semiconductors for photocatalytic and photoelectrochemical water splitting, Chem Soc Rev 43 (2014) 7520-35.

[29] M. M. Momeni, Y. Ghayeb, Fabrication, characterization and photoelectrochemical behavior of Fe-TiO_2 nanotubes composite photoanodes for solar water splitting, Journal of Electroanalytical Chemistry 751 (2015) 43 - 48.

[30] M. M. Momeni, Y. Ghayeb, Visible light-driven photoelectrochemical water splitting on ZnO –TiO_2 heterogeneous nanotube photoanodes, J Appl Electrochem 45 (2015) 557-566.

[31] R. Abe, Recent Progress on Photocatalytic and Photoelectrochemical Water Splitting under Visible Light Irradiation, Journal of Photochemistry and Photobiology C: Photochemistry Reviews 11 (2010) 179-209.

[32] M. M. Momeni, Y. Ghayeb, Z. Ghonchegi, Visible light activity of sulfur-doped TiO_2 nanostructure photoelectrodes prepared by single-step electrochemical anodizing process, J Solid State Electrochem 19 (2015) 1359 -1366.

[33] Y. Lin, G. Yuan, R. Liu, S. Zhou, S. W. Sheehan, D. Wang, Semiconductor nanostructure-based photoelectrochemical water splitting: a brief review, Chemical Physics Letters 507 (2011) 209-215.

[34] M. M. Momeni, Y. Ghayeb, S. Gheibee, Silver nanoparticles decorated titanium dioxide-tungsten trioxide nanotube films with enhanced visible light photo catalytic activity, Ceramics International 43 (2017) 564 -570.

[35] S. Zhang, R. Sakai, T. Abe, T. Iyoda, T. Norimatsu, K. Nagai, Photoelectrochemical and Photocatalytic Properties of Biphasic Organic p- and n-Type Semiconductor Nanoparticles Fabricated by a Reprecipitation Process, ACS Appl. Mater. Interfaces 3 (2011) 1902–1909.

[36] Y. K. Gaudy, S. Haussener, Utilizing modeling, experiments, and statistics for the analysis of water-splitting photoelectrodes, J. Mater. Chem. A 4 (2016) 3100–3114.

[37] N. S. Lewis, Photoeffects at the semiconductor/liquid interface, Ann. Rev. Mater. Sci. 14 (1984) 95-117.

[38] N. B. Chaure, A. P. Samantilleke, R. P. Burton, J. Young, I. M. Dharmadasa, Electrodeposition of p+, p, i, n and n+-type copper indium gallium diselenide for development of multilayer thin film solar cells, Thin Solid Films 472 (2005) 212-216.

[39] A. B. Rohom, P. U. Londhe, N. B. Chaure, The effect of pH and selenization on the properties of $CuInSe_2$ thin films prepared by electrodeposition technique for device applications, J Solid State Electrochem19 (2015) 201-210.

[40] H. Cesiulis, N. Tsyntsaru, A. Ramanavicius, G. Ragoisha, Springer International Publishing Switzerland (2016) DOI 10.1007/978-3-319-30198-3_1.

[41] M. Soestbergen, Frumkin-Butler-Volmer theory and mass transfer in electrochemical cells Russian Journal of Electrochemistry 48 (2012) 570–579.

[42] A. Lasia, Electrochemical Impedance Spectroscopy and its Applications e-book, 2014 Springer, New York.

Table captions

Table 1. Summary of Raman mode frequencies of CIT films.

Table 2. Summary of elemental compositions obtained by EDAX for as-deposited and annealed CIT thin films.

Figure captions

Figure 1 The cyclic voltammogram recorded on FTO substrate at 75 ^{o}C for stirred solution at ~ 150 rpm for co-deposition of Cu, In, Te with citric acid at pH 4.

Figure 2 X-ray diffraction patterns of as-deposited and annealed CIT thin films.

Figure 3 Raman spectra of as-deposited and annealed CIT thin films deposited at -0.7 V and -0.8 V.

Figure 4 Plot of $(\alpha h\nu)^2$ verses Energy ($h\nu$) for as-deposited and annealed CIT films at 400 ^{o}C for 5 minutes deposited at (A) -0.7 V and (B) -0.8 V.

Figure 5 SEM Images of as-deposited CIT films deposited at (a) -0.6 V, (b) -0.7 V, (c) -0.8 V and (d) -0.9 V; and annealed CIT films at 400 ^{o}C for 15 minutes deposited at (e) -0.7 V and (f) -0.8 V respectively.

Figure 6 Energy dispersive X-ray spectra of as-deposited and annealed CIT samples deposited at -0.8 V.

Figure 7 Schematic representation of solid-electrolyte interface. Figure (a) represents the top of the valance band edge energy level (Ev), bottom of the conduction band edge energy level (Ec), Fermi energy (E_f) of p-type semiconductor and redox potential/energy of electrolyte with respect to vacuum level separately. (b) Shows the band bending of the p-type semiconductor kept in contact with electrolyte to equilibrate the Fermi energy of a semiconductor and redox potential of electrolyte. (c) The photoexcitation of p-type semiconductor electrode. (d) Represents the photoexcitation of electrolyte.

Figure 8 Photoelectrochemical (PEC) response of annealed CIT films at 400 ^{o}C for 15 minutes deposited at (a) -0.7 V and (b) – 0.8 V.

Figure 9 Impedance spectroscopy of annealed CIT films at 400 ^{o}C for 15 minutes deposited at (a) -0.7 V and (b) -0.8 V respectively.

Table 1.

Mode	Std. Mode frequencies (cm^{-1})	Mode frequencies (cm^{-1}) in present data			
	Literature data	As-deposited		Annealed	
		-0.7 V	-0.8 V	-0.7 V	-0.8 V
A_1	123	119	117	121	120
E	128	125	125	silent	silent
B^3_1	143	137	137	140	140
E	159	155	155	silent	silent
E^5 and/ or $B_2{}^3$	180	180	silent	silent	silent
E and B_2	267	261	silent	267	266

Table 2.

Deposition Potential (V)	Elemental Composition in At. %			Cu/In ratio	Te/(Cu+In) Ratio
	Cu	In	Te		
- 0.6 (as-deposited)	30	5	65	6.0	1.8
- 0.7 (as-deposited)	19	23	58	0.8	1.4
- 0.8 (as-deposited)	17	31	52	0.6	1.0
- 0.9 (as-deposited)	19	35	46	0.5	0.8
- 0.7 (annealed)	17	25	58	0.7	1.4
- 0.8 (annealed)	16	36	48	0.4	0.9

Graphical abstract

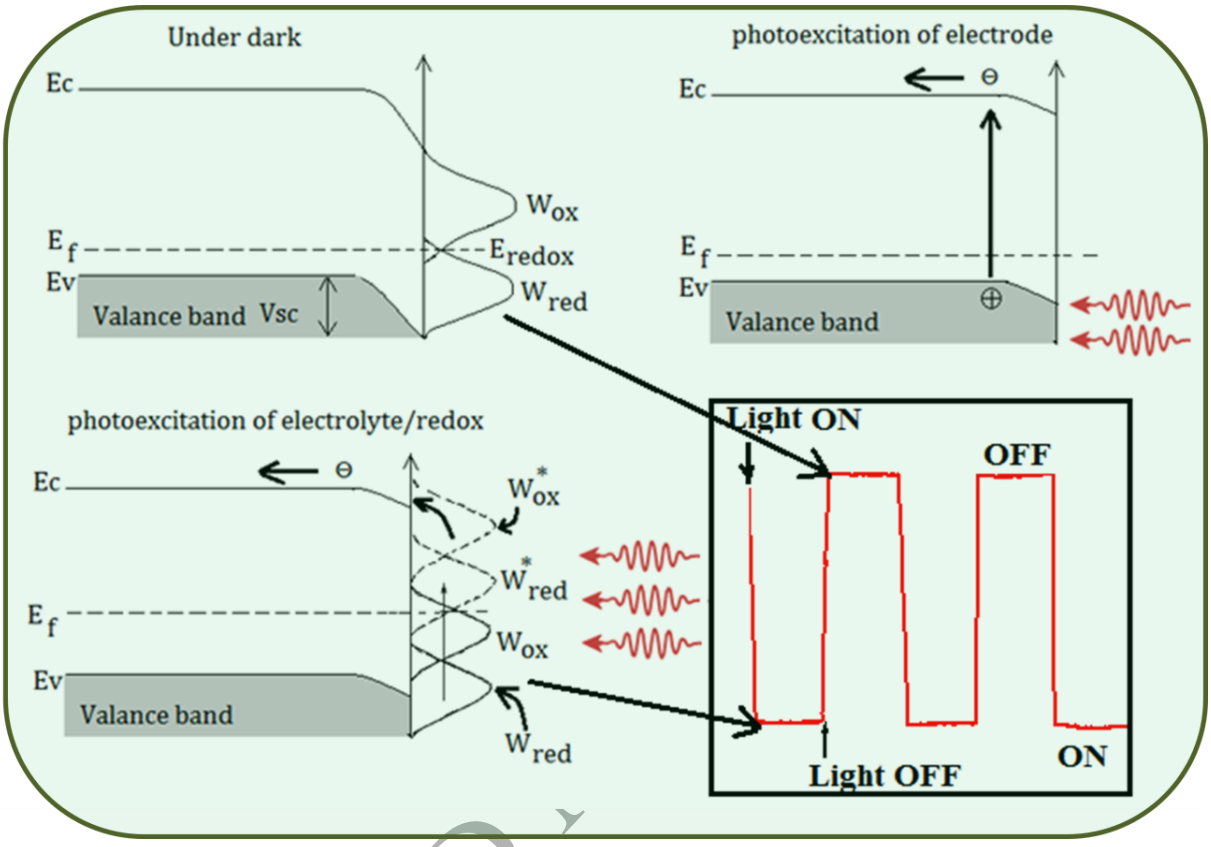

Change in photoelectrochemical (PEC) signal under dark and illuminated conditions